Anisotropic Dirac cone and slow edge states in a photonic Floquet lattice

Yuan Li and Xiankai Sun*

Department of Electronic Engineering, The Chinese University of Hong Kong, Shatin, New Territories, Hong Kong SAR, China

(Received 20 May 2021; revised 17 August 2021; accepted 10 September 2021; published 12 January 2022)

Dirac cones with isotropic and linear dispersion, as in graphene, exhibit ultrahigh carrier mobility and offer an intriguing method to manipulate the behavior of particles. This concept has recently been extended to anisotropic Dirac cones with anisotropic dispersion in condensed matter, but their photonic counterparts are yet to be explored. Here, by introducing anisotropic coupling, we propose a Floquet lattice with a realistic photonic scheme that supports anisotropic Dirac cones and abundant topological phases. Under the highly anisotropic circumstances, the presence of anomalous Floquet insulators is demonstrated, where topological slow edge states are found along a specific direction. The group velocity of the edge states can be tailored continuously by adjusting the anisotropy of the lattice. These slow edge states are robust against disorders and can be harnessed for developing intriguing applications such as anisotropic devices, topological delay lines, and optical nonlinear devices.

DOI: 10.1103/PhysRevB.105.014306

I. INTRODUCTION

Dirac semimetals with a linear energy dispersion at the Fermi level are a novel class of condensed-matter systems that exhibit unconventional transport properties such as ballistic charge transport and ultrahigh carrier mobility [1–4]. The discovery of the Dirac cones, which exist in single-layer graphene [5], ignited intense research interests in Dirac materials in the past decade [6–16]. Consequently, the Dirac cones in graphene have been theoretically extended to highly anisotropic cases with anisotropic dispersion by applying an external periodic potential [17–19]. Recently, anisotropic Dirac cones have been experimentally demonstrated by using high-resolution angle-resolved photoemission spectroscopy in several materials including (Sr/Ca)$MnBi_2$, χ_3 borophene, and B_2S honeycomb monolayer [20–26]. These anisotropic Dirac cone materials have attracted significant attention due to their anisotropic carrier mobility, which leads to applications of direction-dependent transport.

Inspired by the Dirac cone materials in condensed-matter systems, several research groups have realized photonic Dirac semimetals on several platforms [27–31]. For instance, a honeycomb lattice composed of straight waveguides exhibits Dirac cones in its photonic band structure [31], where the waveguide array serves as the optical analog of graphene. Those systems were studied based on a well-known static Hamiltonian preserving "time"-reversal symmetry, where the coordinate z along the propagation direction acts as "time." When a periodic drive is implemented (Floquet engineering) in waveguide arrays, the "time"-reversal symmetry can be broken, leading to bosonic particles whose behavior is profoundly distinct from that in a static system. It has been demonstrated that the Floquet band structure can host unpaired Dirac cones at critical points between different topological phases [32]. More specifically, anomalous Floquet insulators host topologically nontrivial edge states (ESs) in spite of a zero Chern number for all bands [33–36]. While several platforms host photonic Dirac cones and topological insulators, a deterministic scheme of anisotropic Dirac cones and the effect of anisotropy in topological insulators remain largely unexplored.

In this work, we proposed a scheme for realizing anisotropic Dirac cones in a photonic lattice composed of evanescently coupled elliptic-helical waveguides. Due to the periodicity along the propagation direction, the proposed photonic lattice can be mapped into a Floquet model. Unlike previous designs hosting isotropic Dirac cones [32], our scheme hosts anisotropic Dirac cones due to the introduced anisotropic coupling. We reshaped the Dirac cones to anisotropic type by Floquet engineering, and these anisotropic Dirac cones were numerically verified via conical diffraction. Furthermore, the topological transition between trivial insulator (TI) and anomalous Floquet insulator (AFI) was investigated. Generally, a topological transition can occur by detuning isotropic coupling strength or sublattice asymmetry [34,37,38]. Here, we found that lattice anisotropy also plays a significant role in topological transitions and topological edge states. Under high anisotropy, the edge modes at straight edges exhibit diverse propagation behaviors. Interestingly, without reducing the bulk band gap, the group velocity of the edge states can be increased along one direction at the cost of being decreased along its perpendicular direction. This unique transport feature opens the way for engineering topologically protected edge states, which enable new applications in broadband slow-light photonic systems.

II. FLOQUET MODEL AND REALISTIC PHOTONIC IMPLEMENTATION

Let us start our analysis by considering a simple Floquet model as shown in Fig. 1(a). This bipartite square lattice is

*Corresponding author: xksun@cuhk.edu.hk

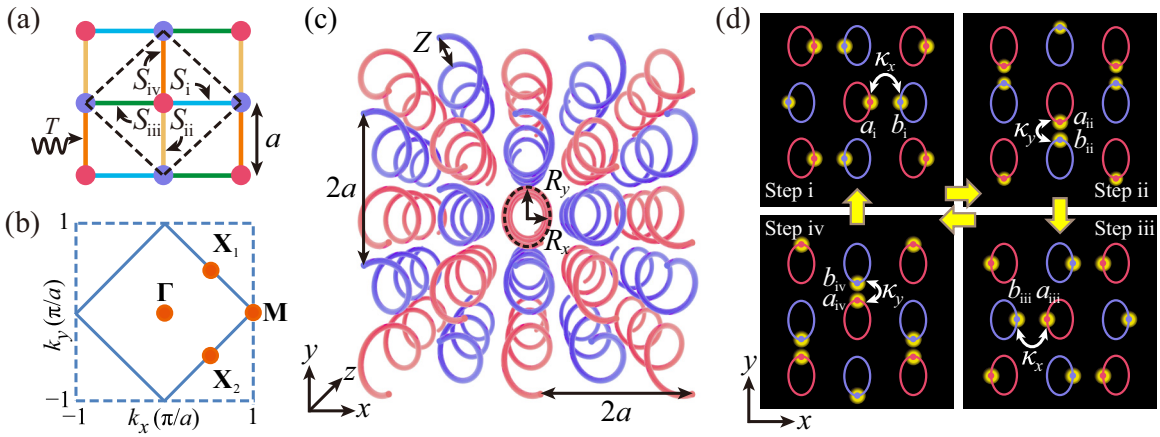

FIG. 1. Floquet system and photonic implementation. (a) Schematic representation of a reduced Floquet lattice composed of sublattice A-type (red dots) and B-type (blue dots) atoms, where the black dashed lines enclose a unit cell. The coupling between neighboring waveguides can be decomposed into four steps. In each step, the evolution of photons is governed by an evolution matrix S_j ($j = \mathrm{i}, \mathrm{ii}, \mathrm{iii}$, and iv). (b) Corresponding Brillouin zone, where the red dots represent high-symmetry points and the blue solid lines enclose the first Brillouin zone. (c) Schematic illustration of a bipartite square lattice composed of evanescently coupled elliptic-helical waveguides. This bipartite square lattice is composed of A-type (red) and B-type (blue) sublattices, twisting counterclockwise along the propagation direction (z axis) with a relative shift. (d) Cross sections of the waveguide lattice showing the coupling between neighboring waveguides in the four steps. In each step, the coupling between the neighboring waveguides occurs only along a specific direction.

composed of two sublattices A and B, where the red (blue) dots represent A-type (B-type) sites, and the bonds denote modulated coupling between neighboring sites with a modulation period T. To simplify the Floquet model, we divide one period into four steps: i, ii, iii, and iv. In each step, the coupling along a specific bond is in effect, and those along the other three bonds remain inactive. The active coupling relation in step j ($= \mathrm{i}, \mathrm{ii}, \mathrm{iii}$, and iv) is described by a scattering matrix S_j, marked by bonds with different colors in Fig. 1(a). Note that the coupling amplitudes are modulated in a chiral way, and S_j serves as the evolution operator over a quarter period, $S_j\boldsymbol{\psi}(t) = \boldsymbol{\psi}(t + T/4)$, where $\boldsymbol{\psi} = (\psi_A, \psi_B)$ is the wave function, and ψ_A (ψ_B) represents the tight-binding amplitude of sublattice A (B). The evolution of particles over one period is governed by $U\boldsymbol{\psi}(t) = \boldsymbol{\psi}(t + T)$, where U is the Floquet evolution operator expressed as $U = S_{\mathrm{iv}}S_{\mathrm{iii}}S_{\mathrm{ii}}S_{\mathrm{i}}$. The lattice basis vectors are $\mathbf{a}_1 = (a, a)$ and $\mathbf{a}_2 = (a, -a)$, where a is the spacing between the sublattices A and B. As a consequence of the spatial translation symmetry, the crystal momenta $\mathbf{k} = (k_x, k_y)$ are good quantum numbers. Figure 1(b) depicts the Brillouin zone associated with the bipartite square lattice, where the blue solid lines enclose the first Brillion zone. The general scattering matrix S_0, which contains the coupling relations, can be expressed as

$$S_0 = \begin{pmatrix} e^{i\Delta}t & -ie^{i\Delta}\kappa \\ -ie^{-i\Delta}\kappa & e^{-i\Delta}t \end{pmatrix}, \tag{1}$$

where $\kappa \in [0, 1]$ is the coupling coefficient, $t \in [0, 1]$ is the transmission coefficient, and Δ is the phase shift arising from the difference of on-site energy between sublattices A and B.

Considering the Bloch phase factors in each step, we derived the complete coupling relations:

$$S_0\begin{pmatrix} a_{\mathrm{i}} \\ b_{\mathrm{i}}e^{i\mathbf{k}\cdot\mathbf{x}} \end{pmatrix} = \begin{pmatrix} a_{\mathrm{ii}} \\ b_{\mathrm{ii}}e^{i\mathbf{k}\cdot\mathbf{x}} \end{pmatrix}, \tag{2}$$

$$S_0\begin{pmatrix} a_{\mathrm{ii}} \\ b_{\mathrm{ii}}e^{-i\mathbf{k}\cdot\mathbf{y}} \end{pmatrix} = \begin{pmatrix} a_{\mathrm{iii}} \\ b_{\mathrm{iii}}e^{-i\mathbf{k}\cdot\mathbf{y}} \end{pmatrix}, \tag{3}$$

$$S_0\begin{pmatrix} a_{\mathrm{iii}} \\ b_{\mathrm{iii}}e^{-i\mathbf{k}\cdot\mathbf{x}} \end{pmatrix} = \begin{pmatrix} a_{\mathrm{iv}} \\ b_{\mathrm{iv}}e^{-i\mathbf{k}\cdot\mathbf{x}} \end{pmatrix}, \tag{4}$$

$$S_0\begin{pmatrix} a_{\mathrm{iv}} \\ b_{\mathrm{iv}}e^{i\mathbf{k}\cdot\mathbf{y}} \end{pmatrix} = \begin{pmatrix} a_{\mathrm{i}} \\ b_{\mathrm{i}}e^{i\mathbf{k}\cdot\mathbf{y}} \end{pmatrix}, \tag{5}$$

where a_j and b_j represent the amplitude of the sublattice A and B, respectively, in step j. With the unit vectors $\mathbf{x} = (a, 0)$ and $\mathbf{y} = (0, a)$, the Bloch phase factors are determined. The general evolution matrix S_j in each step can be expressed in forms of the Bloch waves:

$$S_j(\mathbf{k}\cdot\mathbf{d}) = \begin{pmatrix} e^{i\Delta}t_j & -ie^{i(\Delta+\mathbf{k}\cdot\mathbf{d})}\kappa_j \\ -ie^{-i(\Delta+\mathbf{k}\cdot\mathbf{d})}\kappa_j & e^{-i\Delta}t_j \end{pmatrix}, \tag{6}$$

where $\mathbf{d}$ is $\mathbf{x}$, $-\mathbf{y}$, $-\mathbf{x}$, and $\mathbf{y}$ for steps i, ii, iii, and iv, respectively. As a result, the entire Floquet evolution operator $U(\mathbf{k})$ can be expressed as a product of the four evolution matrices:

$$U(\mathbf{k}) = S_{\mathrm{iv}}(k_y a)S_{\mathrm{iii}}(-k_x a)S_{\mathrm{ii}}(-k_y a)S_{\mathrm{i}}(k_x a). \tag{7}$$

Under the assumption of no scattering loss in each step ($\kappa_j^2 + t_j^2 = 1$), the eigenvalues of the entire Floquet evolution operator U have the form of $e^{i\beta(\mathbf{k})}$, where $\beta(\mathbf{k})$ is the quasienergy of the Floquet band structure. Note that the coupling coefficient κ_j can be different in each step, which is important for obtaining anisotropic Dirac cones. In a simplified model, we assume $S_{\mathrm{i}} = S_{\mathrm{iii}}$ and $S_{\mathrm{ii}} = S_{\mathrm{iv}}$ so that we can define $\kappa_x = \kappa_{\mathrm{i,iii}}$ and $\kappa_y = \kappa_{\mathrm{ii,iv}}$ as direction-dependent coupling coefficients. Since the coupling coefficients κ_x and κ_y serve as the modulation amplitudes of coupling strength, introducing anisotropic coupling ($\kappa_x \neq \kappa_y$) can be regarded as Floquet engineering.

Our proposed Floquet lattice can be implemented in a realistic photonic system, such as femtosecond-laser-written

waveguides in fused silica [39]. In a coupled-waveguide array, the guided light propagates mainly along the longitudinal direction and spreads slowly along the transverse direction as Floquet-Bloch modes, which makes it an ideal platform for experimental verification of the Floquet theory [30,35,36,40–43]. To that end, we proposed a flexible photonic structure corresponding to the bipartite square Floquet lattice as shown in Fig. 1(c). The red (blue) single-mode waveguides form an array aligned along the longitudinal direction z. Under the paraxial approximation and weak-guidance approximation, the light propagating along the z axis in the waveguide array can be described by $E(x, y, z) = \Psi(x, y, z)\exp(ik_0 z - i\omega t)$ (see the Supplemental Material [44]), and the paraxial optical field $\Psi(x, y, z)$ is governed by the Schrödinger-like equation

$$i\partial_z \Psi(x, y, z) = -\frac{1}{2k_0}\left(\partial_x^2 + \partial_y^2\right)\Psi(x,\ y,\ z) - \frac{k_0 \Delta n(x,\ y,\ z)}{n_0}\Psi(x, y, z), \tag{8}$$

where $n_0 = 1.508$ is the refractive index of the ambient medium, $\lambda = 633\,\text{nm}$ is the operating wavelength, $\omega = 2\pi c/\lambda$ is the corresponding optical frequency, c is the speed of light, $k_0 = 2\pi n_0/\lambda$ is the wave number, and $\Delta n(x,\ y,\ z)$ is the refractive index profile of the elliptic-helical waveguides with a helix period of Z. In the cross sections, the centers of the red waveguides move clockwise following elliptic helices according to $x_0(z) = R_x\cos(2\pi z/Z)$ and $y_0(z) = -R_y\sin(2\pi z/Z)$, where R_x and R_y are the semiminor and semimajor axes, respectively ($R_x \leqslant R_y$). The transverse centers of the blue waveguides move along the z axis similarly but with an additional π phase shift, thus following $x_0(z) = -R_x\cos(2\pi z/Z)$ and $y_0(z) = R_y\sin(2\pi z/Z)$. The refractive index profile of each waveguide follows a hyper-Gaussian function $\Delta n(x, y, z) = \Delta n_{\max}\exp(-[(x - x_0)^2/\sigma^2 + (y - y_0)^2/\sigma^2]^3)$, with $\Delta n_{\max} = 2 \times 10^{-3}$ and $\sigma = 2.5\,\mu\text{m}$. The average separation of the nearest waveguide is a, which serves as the spacing between the sublattices A and B in the original Floquet lattice. We numerically simulated and designed the proposed photonic structure by following the theory and simulation for the femtosecond-laser-written photonic structures [39]. By solving Eq. (8) with a finite-difference beam-propagation method, we obtained the numerical results for our designed photonic structure. In the simulation, we chose a to be 20 μm and Z to be 1 cm to ensure minimal waveguide loss. Since the waveguide spacing is varied along the z axis, we assume that the coupling between the neighboring waveguides occurs in four steps [as shown in Fig. 1(d)], acting equivalently as modulation of coupling. The symmetry in our designed structure guarantees $S_{\text{i}} = S_{\text{iii}}$ and $S_{\text{ii}} = S_{\text{iv}}$, where the corresponding coupling coefficients $\kappa_{\text{i,iii}}$ and $\kappa_{\text{ii,iv}}$ can be determined in simulation. With fixed a and Z, the direction-dependent coupling coefficients κ_x and κ_y depend on R_x and R_y respectively, and thus can be engineered by adjusting R_x and R_y. As a result, this photonic implementation can be mapped into the proposed Floquet lattice with the time coordinate t replaced with the propagation distance z.

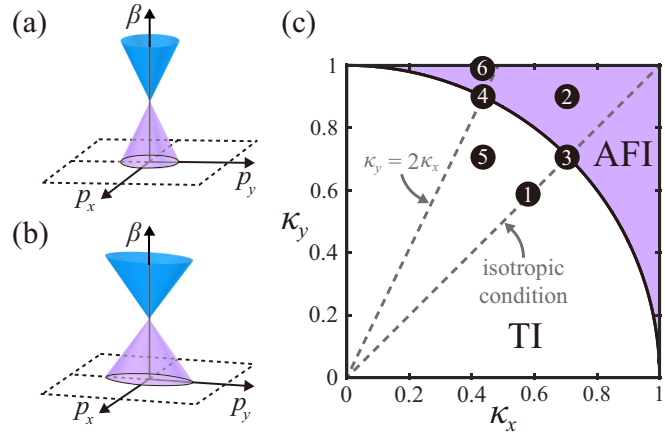

FIG. 2. Schematic illustrations of the Dirac cones and phase diagram. (a) Schematic illustration of an isotropic two-dimensional Dirac cone with symmetric effective velocities ($w_x = w_y$). (b) Schematic illustration of an anisotropic two-dimensional Dirac cone with asymmetric effective velocities ($w_x \neq w_y$). (c) Phase diagram of the Floquet lattice in the case of zero phase shift $\Delta = 0$. TI, trivial insulator; AFI, anomalous Floquet insulator.

III. FLOQUET BAND STRUCTURE AND UNPAIRED DIRAC CONES

With the established Floquet model, we next show how to tune the Floquet lattice into different topological phases and obtain the anisotropic Dirac cones by engineering the coupling coefficients in each step. First, we briefly introduce the anisotropic Dirac cones. Generally, the linearized Dirac Hamiltonian near the Dirac point $\mathbf{Q}$ can be expressed as

$$H_D(\mathbf{p}) = \mathbf{w}_0 \cdot \mathbf{p}I + w_x p_x \sigma_x + w_y p_y \sigma_y, \tag{9}$$

where $\mathbf{p} = \mathbf{k} - \mathbf{Q} = (p_x, p_y)$ is the momentum vector relative to the Dirac point $\mathbf{Q}$, and the effective velocity terms are $\mathbf{w}_0 = (w_{0x}, w_{0y})$, w_x, and w_y. Here the Dirac cones are not tilted with preserved inversion symmetry, and thus the corresponding effective velocity term $\mathbf{w}_0$ is equal to (0, 0). Figures 2(a) and 2(b) show isotropic and anisotropic Dirac cones, respectively. For isotropic Dirac cones, the effective velocity terms w_x and w_y are equal, so the group velocity does not depend on direction. For anisotropic Dirac cones, the effective velocity terms w_x and w_y are unequal, so the group velocity depends on direction.

To obtain anisotropic Dirac cones in our proposed model, we solved for the Floquet band structure $\beta(\mathbf{k})$ and then searched for band crossing which is associated with a topological phase transition [45]. The topological characteristics of our proposed lattice are introduced as follows. In two-dimensional (2D) Floquet systems, zone-edge singularities allow for change of the Chern number of the bands without closing the interzone band gap, which violates the static bulk-edge correspondence. This implies that the Chern number cannot fully characterize the topological properties of Floquet systems [34]. The winding number W_β is suggested as the topological invariant, which characterizes the number of chiral edge modes n_{edge} of an arbitrary Floquet operator U in

a band gap at the quasienergy β:

$$n_{\text{edge}}(\beta) = W_\beta. \tag{10}$$

W_β can be expressed as

$$W_\beta = \frac{1}{8\pi^2}\int dz\, dk_x dk_y \mathrm{Tr}\big(\mathbf{U}_\beta{}^{-1}\partial_z \mathbf{U}_\beta \times \big[\mathbf{U}_\beta{}^{-1}\partial_x \mathbf{U}_\beta, \mathbf{U}_\beta{}^{-1}\partial_y \mathbf{U}_\beta\big]\big), \tag{11}$$

with $U_\beta(\mathbf{k}, z) = U(\mathbf{k}, z)\exp[-iH_{\text{eff}}(\mathbf{k})z]$, where $H_{\text{eff}}(\mathbf{k})$ is defined as $H_{\text{eff}}(\mathbf{k}) = i\ln[U(\mathbf{k}, Z)]/Z$. Based on the Chern number C and winding number W_β, the Floquet systems can be classified into three types: trivial insulators ($C = 0$ and $W_\beta = 0$), Chern insulators ($C \neq 0$ and $W_\beta = 0$), and anomalous Floquet insulators ($C = 0$ and $W_\beta \neq 0$).

To simplify the model, we set zero phase shift $\Delta = 0$ and plot the phase diagram of the Floquet lattice as shown in Fig. 2(c). It is clear that the Floquet system is divided into two topological phases by the critical-phase-transition curve $\arcsin(\kappa_x) + \arcsin(\kappa_y) = \pi/2$. The direction-dependent coupling coefficients κ_x and κ_y play an important role in classification of the topological phases. When the isotropic condition ($\kappa_x = \kappa_y$) is satisfied, the Floquet lattice reduces into the model in Ref. [32]. The systems are classified into trivial insulators for $\arcsin(\kappa_x) + \arcsin(\kappa_y) < \pi/2$ and anomalous Floquet insulators for $\arcsin(\kappa_x) + \arcsin(\kappa_y) > \pi/2$. Figure 3 plots the Floquet band structures $\beta(\mathbf{k})$ solved from the Floquet evolution operator $U(\mathbf{k})$ for several cases. In Fig. 3(a) the system is a trivial insulator with a trivial band gap corresponding to the case marked with ① in Fig. 2(c), while in Fig. 3(b) the system is an anomalous Floquet insulator with a nontrivial band gap corresponding to the case marked with ② in Fig. 2(c). M denotes the quasienergy difference of the two eigenstates at the $\mathbf{\Gamma}$ point, so the size of the band gap is $|M|$. At the phase transition point ($\kappa_x = \kappa_y = \sqrt{2}/2$) marked with ③ in Fig. 2(c), the system hosts an unpaired Dirac cone at the $\mathbf{\Gamma}$ point in the first Brillouin zone, with the corresponding Floquet band structure shown in Fig. 3(c). On the other hand, under the anisotropic condition ($\kappa_x \neq \kappa_y$), this system hosts an anisotropic Dirac cone on the critical-phase-transition curve despite high coupling anisotropy. Without loss of generality, Fig. 3(d) plots the anisotropic Dirac cone for the specific phase transition point [$\arcsin(\kappa_x) = 0.15\pi$ and $\arcsin(\kappa_y) = 0.35\pi$], which is marked with ④ in Fig. 2(c). Expanding the Floquet evolution operator near the $\mathbf{\Gamma}$ point $U \approx \exp[-i(H-\pi)]$, we derived an effective Hamiltonian $H(\mathbf{p})$:

$$H_{\text{eff}}(\mathbf{p}) = 2\kappa_y p_x \sigma_x + 2\kappa_x p_y \sigma_y + \frac{M}{2}\sigma_z, \tag{12}$$

where the effective velocity terms are $w_x = 2\kappa_y$, $w_y = 2\kappa_x$, and M takes the value of $4\arcsin(\kappa_x) + 4\arcsin(\kappa_y) - 2\pi$. The effective Hamiltonian $H_{\text{eff}}(\mathbf{p})$ reduces to a Dirac Hamiltonian for $M = 0$. Therefore, the critical-phase-transition curve [$\arcsin(\kappa_x) + \arcsin(\kappa_y) = \pi/2$] can also be identified based on the vanishing M. Note that the difference in κ_x and κ_y induces the anisotropic Dirac cone with different group velocities along the x and y directions. The group velocity of the Dirac cone can be enhanced along one direction at the cost of being reduced along its perpendicular direction. Figures 3(e) and 3(f) plot the equifrequency surfaces of

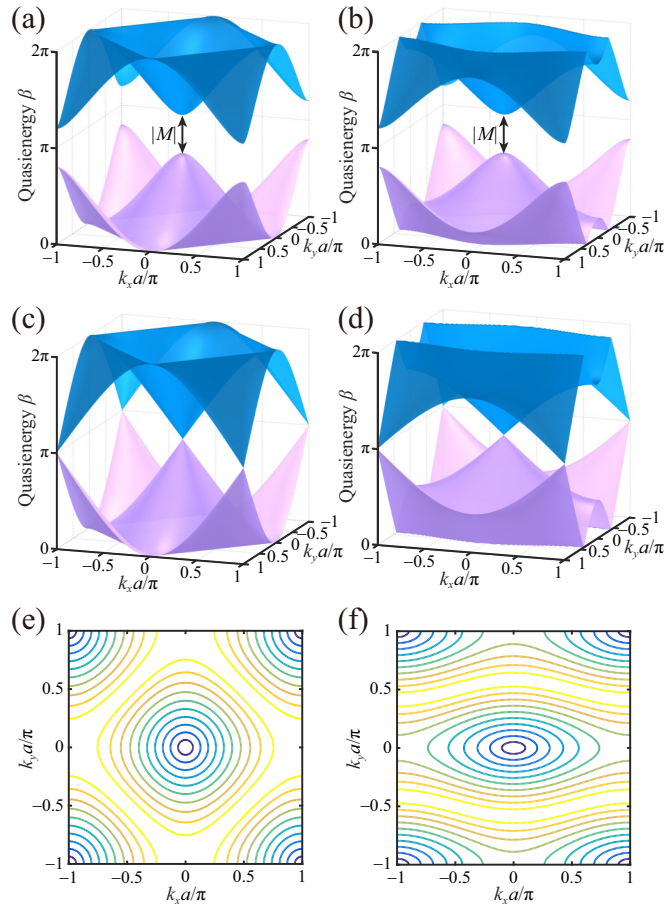

FIG. 3. Floquet band structures for different topological phases and equifrequency contours for the corresponding Dirac cones. (a) Band structure of a trivial insulator [$\arcsin(\kappa_x) = \arcsin(\kappa_y) = 0.2\pi$, $|M| = 0.2\pi$] with a trivial band gap. (b) Band structure of an anomalous Floquet insulator [$\arcsin(\kappa_x) = 0.25\pi$, $\arcsin(\kappa_y) = 0.35\pi$, $|M| = 0.2\pi$] with a nontrivial band gap. (c) Band structure of a critical-phase-transition point ($\kappa_x = \kappa_y = \sqrt{2}/2$), which hosts an isotropic Dirac cone under the isotropic condition. (d) Band structure of another critical-phase-transition point [$\arcsin(\kappa_x) = 0.15\pi$ and $\arcsin(\kappa_y) = 0.35\pi$], which hosts an anisotropic Dirac cone under the anisotropic condition. (e) Equifrequency contours for the isotropic Dirac cone, which exhibits a circular shape at the Dirac point $\mathbf{\Gamma}$. (f) Equifrequency contours for the anisotropic Dirac cone, which exhibits an elliptic shape at the Dirac point $\mathbf{\Gamma}$.

the isotropic and anisotropic 2D Dirac cones, respectively. For the isotropic Dirac cone in Fig. 3(c), the equifrequency surfaces are composed of a set of circles whose radii decrease linearly until reaching zero at the Dirac point $\mathbf{\Gamma}$. By contrast, for an anisotropic Dirac cone in Fig. 3(d), the equifrequency surfaces are composed of a set of ellipses whose semimajor and semiminor axes decrease linearly until reaching zero at the Dirac point $\mathbf{\Gamma}$.

IV. PROPAGATION BEHAVIOR OF AN ANISOTROPIC DIRAC CONE

With the anisotropic Dirac cone obtained in the photonic lattice, we next investigated the unique propagation behavior

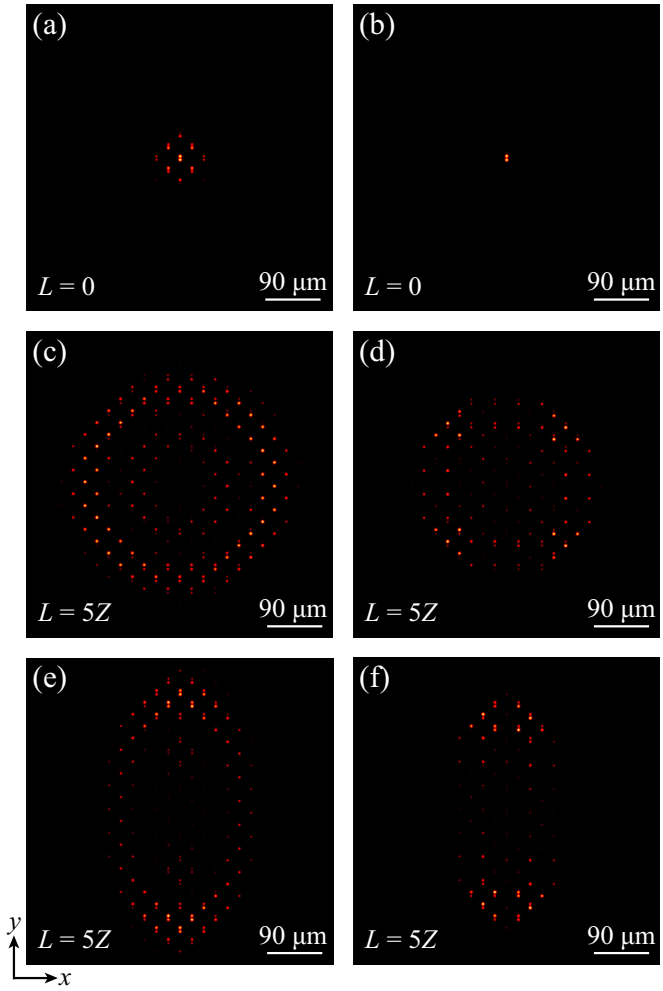

FIG. 4. Comparison of conical diffraction between isotropic and anisotropic Dirac cones. (a),(b) Initial excitation by a Gaussian beam (a) and single-unit-cell beam (b). (c),(e) Numerically simulated output intensity profile $|\Psi(x, y, L)|^2$ of the Floquet lattice for an isotropic Dirac cone (c) and for an anisotropic Dirac cone (e) under initial excitation of a Gaussian beam. (d),(f) Numerically simulated output intensity profile $|\Psi(x, y, L)|^2$ of the Floquet lattice for an isotropic Dirac cone (d) and for an anisotropic Dirac cone (f) under initial excitation of a single-unit-cell beam. Both lattices contain 12 × 12 unit cells, and the propagation distance is $L = 5Z$.

of these Dirac cones. Conical diffraction can prove the existence of a Dirac cone [46]. When an initial wave packet of a Dirac cone state is excited, it will evolve into a ring shape under linear relativistic dispersion, which is known as conical diffraction. For honeycomb lattices with two Dirac cones located at **K** and **K**′, a spatially structured input beam is needed to selectively excite one cone to show conical diffraction [41]. With the unpaired Dirac cones at the **Γ** point, a conical diffraction pattern can be generated by a normally incident unstructured Gaussian beam. Figure 4 presents the numerically simulated results of conical diffraction in our proposed scheme by solving the paraxial equation [Eq. (8)]. To demonstrate the conical diffraction, we excited a broad Gaussian beam as shown in Fig. 4(a) as the input profile. Note that the Floquet eigenmodes in the longitudinal (z) direction are equivalent to the Bloch modes in the transverse (x−y) plane, which is simply a superposition of a set of single-waveguide excitations. The corresponding output profiles for the isotropic and anisotropic Dirac cone are displayed in Figs. 4(c) and 4(e), respectively. For the isotropic Dirac cone ($\kappa_x = \kappa_y = \sqrt{2}/2$, $R_x = R_y = 6.45\,\mu$m), a conventional conical diffraction pattern can be observed after a propagation distance $L = 5Z$. When the isotropic Dirac cone is excited, the conical diffraction takes the shape of a circular ring with a constant thickness during propagation. By contrast, for the anisotropic Dirac cone, the conical diffraction pattern is no longer a circular ring because of the direction-dependent group velocity $v_g = -d\beta/dk$. Note that for the case of $2\kappa_x = \kappa_y$ ($2v_{xg} = v_{yg}$, $R_x = 6.0\,\mu$m, $R_y = 6.8\,\mu$m), the transverse displacement of the wave packet along the $+y$ ($-y$) direction is twice that along the $+x$ ($-x$) direction, thus exhibiting an elliptic profile, which indicates that the group velocity is locked to the propagation direction.

Additionally, if the input beam size is comparable to the period a of the discrete system (narrow-beam cases), the well-known discrete propagation patterns arise, which are profoundly different from those in continuous systems. An extreme case of narrow-beam excitation is displayed in Fig. 4(b), where only a single unit cell was excited. The corresponding output discrete conical-like diffraction patterns for the isotropic and anisotropic Dirac cone are displayed in Figs. 4(d) and 4(f), respectively, which reveal the unique propagation behavior of the Floquet Dirac cones (see Supplementary Video 1). These discrete conical-like diffraction patterns exhibit a dark central spot, indicating that the group velocity is nonzero almost everywhere. For the isotropic Dirac cone ($\kappa_x = \kappa_y$), a discrete diffraction pattern arises because the Floquet spectrum is periodic along the quasienergy β axis and there is no flat band edge [32]. For the anisotropic Dirac cone ($\kappa_x \neq \kappa_y$), although a flat band edge arises at the high-symmetry **M** points, the single-unit-cell beam mainly excited modes near the Dirac point (i.e., the **Γ** point), so the discrete conical-like diffraction pattern is preserved. The dynamic propagation behaviors of conical diffraction for both broad and narrow excitations are displayed in Supplementary Video 1.

V. TOPOLOGICAL TRANSITION AND SLOW EDGE STATES

In this section, we demonstrate topological transition and manipulation of group velocity of the chiral edge states by adjusting the direction-dependent coupling coefficients. As discussed above, the coupling coefficients along the x and y directions determine the topological phases of the proposed lattice, and the chiral edge states are preserved despite high anisotropy of coupling coefficients. Next, we will investigate how these chiral edge states are influenced by the degree of anisotropy.

To characterize the topological feature of our proposed model, we first considered a stripe structure that is periodic in the x direction and terminates at a straight edge, as shown in Fig. 5(a). This stripe structure can be regarded as a supercell of N unit cells. To obtain the Floquet band diagram of this stripe structure, we derived a Floquet evolution operator U_{sc}

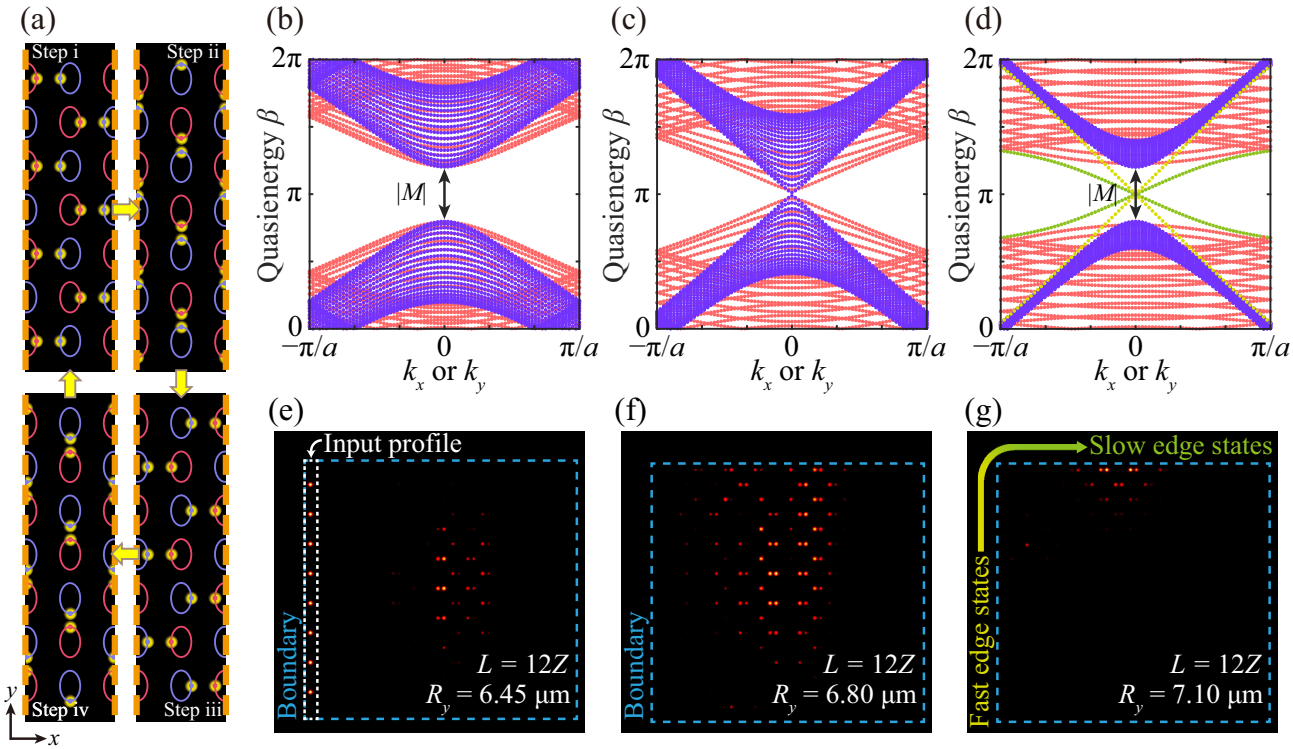

FIG. 5. Topological transition and edge-state band structures. (a) Schematic representation of a stripe structure composed of seven unit cells, where the orange dashed lines represent the periodic boundary. (b)–(d) Edge-state band structures $\beta(\mathbf{k})$ along the x (red) and y (blue) directions with fixed $\arcsin(\kappa_x) = 0.15\pi$ ($R_x = 6.0\,\mu$m), for a trivial insulator with $\arcsin(\kappa_y) = 0.25\pi$ and $|M| = 0.4\pi$ ($R_y = 6.45\,\mu$m) (b), for a critical phase with $\arcsin(\kappa_y) = 0.35\pi$ and $|M| = 0$ ($R_y = 6.80\,\mu$m) (c), and for an anomalous Floquet insulator with $\arcsin(\kappa_y) = 0.45\pi$ and $|M| = 0.4\pi$ ($R_y = 7.10\,\mu$m) (d). In (d) the yellow (green) dots plot the fast (slow) edge states with a larger (smaller) group velocity. (e)–(g) Numerically simulated output intensity profile $|\Psi(x, y, L)|^2$ for different topological phases. The blue dashed boxes represent the boundary of the lattice, and the white dashed box indicates the initial excitation distribution for (e)–(g). With the majority of edge states excited initially around $k_y = 0$, the output intensity profiles exhibit diverse propagation behaviors. Note that the fast edge states along the y direction convert adiabatically into the slow edge states along the x direction around the corner.

for this supercell. Let the wave amplitude vector be $|\psi\rangle = (a_{j,1}, b_{j,1}, \ldots, a_{j,n}, b_{j,n}, \ldots, a_{j,N}, b_{j,N})$ for the supercell in step j, where n is the serial number of the sites. When the serial number n is odd, the coupling relations can be expressed as

$$S_0\begin{pmatrix} a_{\mathrm{i},n} \\ b_{\mathrm{i},n} \end{pmatrix} = \begin{pmatrix} a_{\mathrm{ii},n} \\ b_{\mathrm{ii},n} \end{pmatrix}, \tag{13}$$

$$S_0\begin{pmatrix} a_{\mathrm{ii},n} \\ b_{\mathrm{ii},n+y} \end{pmatrix} = \begin{pmatrix} a_{\mathrm{iii},n} \\ b_{\mathrm{iii},n+y} \end{pmatrix}, \tag{14}$$

$$S_0\begin{pmatrix} a_{\mathrm{iii},n} \\ b_{\mathrm{iii},n+x} \end{pmatrix} = \begin{pmatrix} a_{\mathrm{iv},n} \\ b_{\mathrm{iv},n+x} \end{pmatrix}, \tag{15}$$

$$S_0\begin{pmatrix} a_{\mathrm{iv},n} \\ b_{\mathrm{iv},n-y} \end{pmatrix} = \begin{pmatrix} a_{\mathrm{i},n} \\ b_{\mathrm{i},n-y} \end{pmatrix}. \tag{16}$$

When the serial number n is even, the coupling relations can be expressed as

$$S_0\begin{pmatrix} a_{\mathrm{i},n} \\ b_{\mathrm{i},n-x} \end{pmatrix} = \begin{pmatrix} a_{\mathrm{ii},n} \\ b_{\mathrm{ii},n-x} \end{pmatrix}, \tag{17}$$

$$S_0\begin{pmatrix} a_{\mathrm{ii},n} \\ b_{\mathrm{ii},n+y} \end{pmatrix} = \begin{pmatrix} a_{\mathrm{iii},n} \\ b_{\mathrm{iii},n+y} \end{pmatrix}, \tag{18}$$

$$S_0\begin{pmatrix} a_{\mathrm{iii},n} \\ b_{\mathrm{iii},n} \end{pmatrix} = \begin{pmatrix} a_{\mathrm{iv},n} \\ b_{\mathrm{iv},n} \end{pmatrix}, \tag{19}$$

$$S_0\begin{pmatrix} a_{\mathrm{iv},n} \\ b_{\mathrm{iv},n-y} \end{pmatrix} = \begin{pmatrix} a_{\mathrm{i},n} \\ b_{\mathrm{i},n-y} \end{pmatrix}. \tag{20}$$

On the stripe's straight edges, the boundary conditions are $e^{i\Delta}a_{\mathrm{ii},N} = a_{\mathrm{iii},N}$, $e^{-i\Delta}b_{\mathrm{ii},1} = b_{\mathrm{iii},1}$, $e^{i\Delta}a_{\mathrm{iv},1} = a_{\mathrm{i},1}$, and $e^{-i\Delta}b_{\mathrm{iv},N} = b_{\mathrm{i},N}$. Due to the translational invariance of the lattice in the x direction, these coupling relations can be reordered to obtain a Bloch-form evolution operator $U_{\mathrm{sc}}(k_x)$ for the supercell, which produces the Floquet edge band structures $\beta(\mathbf{k})$ in Figs. 5(b)–5(d).

The Floquet edge band structures $\beta(\mathbf{k})$ along the x (red) and y (blue) directions are plotted under several special cases as shown in Figs. 5(b)–5(d), with their parameters corresponding to the states marked with ⑤, ④, and ⑥ in Fig. 2(c), respectively. With fixed κ_x and increasing κ_y, Figs. 5(b)–5(d) show that the lattice undergoes a transition from a trivial insulator to an anomalous Floquet insulator accompanied by closing and reopening of the band gap. In Fig. 5(b), the lattice is a trivial insulator with a small value of κ_y, where no chiral edge state exists in the band gap. Increasing the value of κ_y induces the

emergence of the chiral edge states [green and yellow curves in Fig. 5(d)] in a single band gap, implying that the lattice has turned into an anomalous Floquet insulator. The topological transition can be verified experimentally from beam propagation characterization. Here, we numerically simulated the topological transition in our proposed scheme by solving the paraxial equation [Eq. (8)], with the results shown in Figs. 5(e)–5(g) and Supplementary Video 2. To avoid the excitation beam being scattered into the bulk, we excited the edge states at the center of the edge band structure ($\beta \approx \pi$) within a complete band gap. By using a broad beam with initial excitation along the edge [in the area enclosed by the white dashed box in Fig. 5(e)], we could excite the states mainly at the specific momentum $k_y = 0$ in the band structure. With a small R_y, the lattice is in the trivial phase, and thus the excitation spreads directly into the bulk as shown in Fig. 5(e). With a larger R_y (or increased κ_y), as shown in Fig. 5(g), the beam propagates unidirectionally along the edge, indicating a topological transition.

Next, we investigated the effect of anisotropy on the anomalous topological edge states. For an isotropic lattice ($\kappa_x = \kappa_y$), the edge states exhibit identical propagation behaviors along the x and y directions due to the lattice invariance under the C_4 transformation, where a $\pi/2$ rotation is performed around the z axis. Interestingly, under the highly anisotropic condition ($\kappa_x \ll \kappa_y$), the chiral edge states along the x (green dots) and y (yellow dots) directions exhibit diverse propagation behaviors, with a tradeoff between the transverse group velocities of the edge states along the two orthogonal directions, as shown in Fig. 5(d). Note that the zigzag edges in Refs. [32,43] can be regarded as a mixture of straight edges along the two orthogonal directions in our proposal. As a result, the edge states on zigzag edges exhibit isotropic group velocity even under an anisotropic condition ($\kappa_x \neq \kappa_y$). Additionally, compared with the tightly confined edge states with a high group velocity, those with a low group velocity exhibit broad spatial distributions in the bulk. Despite significant difference between the chiral edge states along the two orthogonal directions, the edge states along the y direction convert adiabatically into those along the x direction around the corner. With increased lattice anisotropy and fixed bulk band gap as determined by $|M|$, the transverse group velocity of the chiral edge states along the direction with a smaller (larger) coupling coefficient becomes lower (higher). To compare the transverse group velocities of the fast (slow) edge states along the two orthogonal directions, we excited the corresponding edge states as shown in the upper panels of Figs. 6(a) and 6(b). The lower panels of Figs. 6(a) and 6(b) display the output profiles of the edge states after a propagation distance $L = 4Z$ (see Supplementary Video 3). The transverse displacement of the slow edge states is approximately half that of the fast edge states, implying that the group velocity is effectively reduced. Additionally, the group velocity of these slow edge states can be tailored continuously by tuning the anisotropic coupling coefficients κ_x and κ_y (see the Supplemental Material [44]). Note that under the highly anisotropic condition ($\kappa_x \ll \kappa_y$), our slow edge states exhibit an even lower group velocity than those in Ref. [36].

The topological slow light offers distinct advantages over the traditional slow-light systems [47]. In traditional slow-light systems, reduction of group velocity usually comes at the expense of bandwidth. In our proposed scheme, by engineering the lattice anisotropy, the group velocity of the edge states along a specific direction can be reduced without reducing the bandwidth, thereby generating broadband topological slow-light states. Another well-known challenge in traditional slow-light systems is the enhanced disorder-induced backscattering, loss, and localization. The topological slow-light system has additional advantages in dynamic propagation of edge states when an edge defect is introduced by removing a single waveguide. Figures 6(c) and 6(d) show that both types of edge states along the two orthogonal directions have unobstructed propagation through the edge defect under the highly anisotropic condition, implying that the topological edge states are robust against defects (see Supplementary Videos 4 and 5). Note that the edge defect forms a small zigzag edge termination, which supports topological edge states, and an arbitrary edge is a mixture of straight and zigzag edges. Figure 6(e) and Supplementary Video 6 show the dynamic propagation of the edge states along an arbitrary edge, which demonstrates their topological robustness.

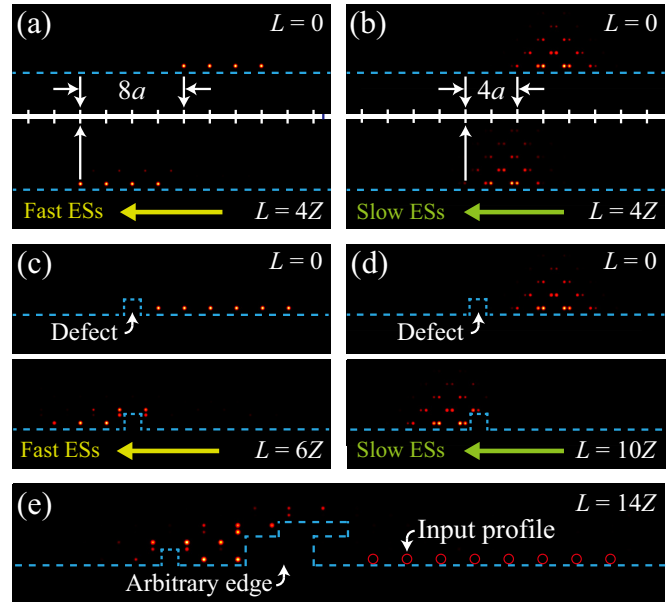

FIG. 6. Numerically simulated dynamic propagation of the edge states. (a),(b) Dynamic propagation of the edge states with a larger group velocity (a) and a smaller group velocity (b). The unit scale of the ruler is $2a$, and the blue dashed lines represent the boundary. (c),(d) Dynamic propagation of the edge states with a larger group velocity (c) and a smaller group velocity (d) when a defect is introduced on the edge. (e) Dynamic propagation of the edge states along an arbitrary edge.

VI. DISCUSSION AND CONCLUSION

In conclusion, we have proposed a Floquet lattice and a realistic photonic scheme to investigate anisotropic Dirac cones in the bosonic domain by introducing anisotropy. With appropriately designed lattice anisotropy, the slope of the Dirac cone along a specific direction can be engineered continuously. Consequently, one can tune the isotropic Dirac cone

into an anisotropic type. We have demonstrated the existence of the isotropic and anisotropic Dirac cones in our proposed Floquet model via conical diffraction. Additionally, the lattice anisotropy also plays an important role in topological transitions and topological edge states. Under specific settings, light can propagate unidirectionally along edges, which indicates the presence of anomalous Floquet insulators. The dynamic propagation behaviors show that the transverse group velocities of these edge states can be reduced effectively, thereby generating broadband topological slow light. Since the coupled-waveguide array in our proposed scheme is theoretically equivalent to a microring lattice [48], our results may inspire applications in optical delay lines as well as enhanced light–matter interactions and optical nonlinearities. Compared with traditional slow-light systems, the topological edge states in this proposal are more reliable because of their high robustness against local perturbations. These findings may also offer new insights into dispersion engineering for future studies concerning continuous media and hyperbolic metamaterials [49–54].

ACKNOWLEDGMENTS

This work was supported by the Research Grants Council of Hong Kong (No. 14209519). The authors acknowledge valuable comments and suggestions from Fahimeh Dehghan, Carnegie Mellon University and Zhen Zhang, Huazhong University of Science and Technology.

[1] K. S. Novoselov, A. K. Geim, S. V. Morozov, D. Jiang, M. I. Katsnelson, I. V. Grigorieva, S. V. Dubonos, and A. A. Firsov, Two-dimensional gas of massless Dirac fermions in graphene, Nature (London) **438**, 197 (2005).

[2] Y. B. Zhang, Y. W. Tan, H. L. Stormer, and P. Kim, Experimental observation of the quantum Hall effect and Berry's phase in graphene, Nature (London) **438**, 201 (2005).

[3] A. H. Castro Neto, F. Guinea, N. M. R. Peres, K. S. Novoselov, and A. K. Geim, The electronic properties of graphene, Rev. Mod. Phys. **81**, 109 (2009).

[4] A. K. Geim, Graphene: Status and prospects, Science **324**, 1530 (2009).

[5] K. S. Novoselov, A. K. Geim, S. V. Morozov, D. Jiang, Y. Zhang, S. V. Dubonos, I. V. Grigorieva, and A. A. Firsov, Electric field effect in atomically thin carbon films, Science **306**, 666 (2004).

[6] T. O. Wehling, A. M. Black-Schaffer, and A. V. Balatsky, Dirac materials, Adv. Phys. **63**, 1 (2014).

[7] Z. K. Liu, B. Zhou, Y. Zhang, Z. J. Wang, H. M. Weng, D. Prabhakaran, S. K. Mo, Z. X. Shen, Z. Fang, X. Dai, Z. Hussain, and Y. L. Chen, Discovery of a three-dimensional topological Dirac semimetal, Na_3Bi, Science **343**, 864 (2014).

[8] S. M. Young and C. L. Kane, Dirac Semimetals in Two Dimensions, Phys. Rev. Lett. **115**, 126803 (2015).

[9] Z. J. Wang, H. M. Weng, Q. S. Wu, X. Dai, and Z. Fang, Three-dimensional Dirac semimetal and quantum transport in Cd_3As_2, Phys. Rev. B **88**, 125427 (2013).

[10] X. F. Zhou, X. Dong, A. R. Oganov, Q. Zhu, Y. J. Tian, and H. T. Wang, Semimetallic Two-Dimensional Boron Allotrope with Massless Dirac Fermions, Phys. Rev. Lett. **112**, 085502 (2014).

[11] K. H. Liu, L. M. Zhang, T. Cao, C. H. Jin, D. A. Qiu, Q. Zhou, A. Zettl, P. D. Yang, S. G. Louie, and F. Wang, Evolution of interlayer coupling in twisted molybdenum disulfide bilayers, Nat. Commun. **5**, 4966 (2014).

[12] X. M. Wang, A. M. Jones, K. L. Seyler, V. Tran, Y. C. Jia, H. Zhao, H. Wang, L. Yang, X. D. Xu, and F. N. Xia, Highly anisotropic and robust excitons in monolayer black phosphorus, Nat. Nanotechnol. **10**, 517 (2015).

[13] J. Kim, S. S. Baik, S. H. Ryu, Y. Sohn, S. Park, B. G. Park, J. Denlinger, Y. Yi, H. J. Choi, and K. S. Kim, Observation of tunable band gap and anisotropic Dirac semimetal state in black phosphorus, Science **349**, 723 (2015).

[14] B. Wang, S. J. Yuan, Y. H. Li, L. Shi, and J. L. Wang, A new Dirac cone material: A graphene-like Be_3C_2 monolayer, Nanoscale **9**, 5577 (2017).

[15] X. Tang, W. G. Sun, C. Lu, L. Z. Kou, and C. F. Chen, Atomically thin NiB_6 monolayer: A robust Dirac material, Phys. Chem. Chem. Phys. **21**, 617 (2019).

[16] P. Swatek, Y. Wu, L. L. Wang, K. Lee, B. Schrunk, J. Q. Yan, and A. Kaminski, Gapless Dirac surface states in the antiferromagnetic topological insulator $MnBi_2Te_4$, Phys. Rev. B **101**, 161109(R) (2020).

[17] C. H. Park, L. Yang, Y. W. Son, M. L. Cohen, and S. G. Louie, Anisotropic behaviours of massless Dirac fermions in graphene under periodic potentials, Nat. Phys. **4**, 213 (2008).

[18] C. H. Park, L. Yang, Y. W. Son, M. L. Cohen, and S. G. Louie, New Generation of Massless Dirac Fermions in Graphene Under External Periodic Potentials, Phys. Rev. Lett. **101**, 126804 (2008).

[19] C. H. Park, Y. W. Son, L. Yang, M. L. Cohen, and S. G. Louie, Landau Levels and Quantum Hall Effect in Graphene Superlattices, Phys. Rev. Lett. **103**, 046808 (2009).

[20] J. Park, G. Lee, F. Wolff-Fabris, Y. Y. Koh, M. J. Eom, Y. K. Kim, M. A. Farhan, Y. J. Jo, C. Kim, J. H. Shim, and J. S. Kim, Anisotropic Dirac Fermions in a Bi Square Net of $SrMnBi_2$, Phys. Rev. Lett. **107**, 126402 (2011).

[21] S. Tang and M. S. Dresselhaus, Constructing anisotropic single-Dirac-cones in $Bi_{1-x}Sb_x$ thin films, Nano Lett. **12**, 2021 (2012).

[22] G. Lee, M. A. Farhan, J. S. Kim, and J. H. Shim, Anisotropic Dirac electronic structures of $AMnBi_2$ (A = Sr, Ca), Phys. Rev. B **87**, 245104 (2013).

[23] B. J. Feng, J. Zhang, S. Ito, M. Arita, C. Cheng, L. Chen, K. Wu, F. Komori, O. Sugin, K. Miyamoto, T. Okuda, S. Meng, and I. Matsuda, Discovery of 2D anisotropic Dirac cones, Adv. Mater. **30**, 1704025 (2018).

[24] Y. Zhao, X. Y. Li, J. Y. Liu, C. Z. Zhang, and Q. Wang, A new anisotropic Dirac cone material: A B_2S honeycomb monolayer, J. Phys. Chem. Lett. **9**, 1815 (2018).

[25] J. K. Lyu, W. X. Ji, S. F. Zhang, C. W. Zhang, and P. J. Wang, Two-dimensional honeycomb B_2Se with orthogonal lattice: High stability and strong anisotropic Dirac cone, J. Phys. Chem. C **124**, 7558 (2020).

[26] Y. Feng, Z. J. Wang, C. Y. Chen, Y. G. Shi, Z. J. Xie, H. M. Yi, A. J. Liang, S. L. He, J. F. He, Y. Y. Peng, X. Liu, Y. Liu,

L. Zhao, G. D. Liu, X. L. Dong, J. Zhang, C. T. Chen, Z. Y. Xu, X. Dai, Z. Fang, and X. J. Zhou, Strong anisotropy of Dirac cones in $SrMnBi_2$ and $CaMnBi_2$ revealed by angle-resolved photoemission spectroscopy, Sci. Rep. **4**, 5385 (2014).

[27] D. Z. Han, Y. Lai, J. Zi, Z. Q. Zhang, and C. T. Chan, Dirac Spectra and Edge States in Honeycomb Plasmonic Lattices, Phys. Rev. Lett. **102**, 123904 (2009).

[28] S. Bittner, B. Dietz, M. Miski-Oglu, P. O. Iriarte, A. Richter, and F. Schafer, Observation of a Dirac point in microwave experiments with a photonic crystal modeling graphene, Phys. Rev. B **82**, 014301 (2010).

[29] M. Bellec, U. Kuhl, G. Montambaux, and F. Mortessagne, Topological Transition of Dirac Points in a Microwave Experiment, Phys. Rev. Lett. **110**, 033902 (2013).

[30] M. C. Rechtsman, J. M. Zeuner, Y. Plotnik, Y. Lumer, D. Podolsky, F. Dreisow, S. Nolte, M. Segev, and A. Szameit, Photonic Floquet topological insulators, Nature (London) **496**, 196 (2013).

[31] Y. Plotnik, M. C. Rechtsman, D. H. Song, M. Heinrich, J. M. Zeuner, S. Nolte, Y. Lumer, N. Malkova, J. J. Xu, A. Szameit, Z. G. Chen, and M. Segev, Observation of unconventional edge states in 'photonic graphene,' Nat. Mater. **13**, 57 (2014).

[32] D. Leykam, M. C. Rechtsman, and Y. D. Chong, Anomalous Topological Phases and Unpaired Dirac Cones in Photonic Floquet Topological Insulators, Phys. Rev. Lett. **117**, 013902 (2016).

[33] T. Kitagawa, E. Berg, M. Rudner, and E. Demler, Topological characterization of periodically driven quantum systems, Phys. Rev. B **82**, 235114 (2010).

[34] M. S. Rudner, N. H. Lindner, E. Berg, and M. Levin, Anomalous Edge States and the Bulk-Edge Correspondence for Periodically Driven Two-Dimensional Systems, Phys. Rev. X **3**, 031005 (2013).

[35] L. J. Maczewsky, J. M. Zeuner, S. Nolte, and A. Szameit, Observation of photonic anomalous Floquet topological insulators, Nat. Commun. **8**, 13756 (2017).

[36] S. Mukherjee, A. Spracklen, M. Valiente, E. Andersson, P. Ohberg, N. Goldman, and R. R. Thomson, Experimental observation of anomalous topological edge modes in a slowly driven photonic lattice, Nat. Commun. **8**, 13918 (2017).

[37] G. Q. Liang and Y. D. Chong, Optical Resonator Analog of a Two-Dimensional Topological Insulator, Phys. Rev. Lett. **110**, 203904 (2013).

[38] M. Pasek and Y. D. Chong, Network models of photonic Floquet topological insulators, Phys. Rev. B **89**, 075113 (2014).

[39] A. Szameit and S. Nolte, Discrete optics in femtosecond-laser-written photonic structures, J. Phys. B **43**, 163001 (2010).

[40] H. S. Eisenberg, Y. Silberberg, R. Morandotti, and J. S. Aitchison, Diffraction Management, Phys. Rev. Lett. **85**, 1863 (2000).

[41] Q. Q. Cheng, Y. M. Pan, H. Q. Wang, C. S. Zhang, D. Yu, A. Gover, H. J. Zhang, T. Li, L. Zhou, and S. N. Zhu, Observation of Anomalous π Modes in Photonic Floquet Engineering, Phys. Rev. Lett. **122**, 173901 (2019).

[42] Z. J. Yang, E. Lustig, Y. Lumer, and M. Segev, Photonic Floquet topological insulators in a fractal lattice, Light Sci. Appl. **9**, 128 (2020).

[43] J. Noh, S. Huang, D. Leykam, Y. D. Chong, K. P. Chen, and M. C. Rechtsman, Experimental observation of optical Weyl points and Fermi arc-like surface states, Nat. Phys. **13**, 611 (2017).

[44] See Supplemental Material at http://link.aps.org/supplemental/10.1103/PhysRevB.105.014306 for additional information.

[45] J. Cayssol, B. Dora, F. Simon, and R. Moessner, Floquet topological insulators, Phys. Status Solidi RRL **7**, 101 (2013).

[46] O. Peleg, G. Bartal, B. Freedman, O. Manela, M. Segev, and D. N. Christodoulides, Conical Diffraction and Gap Solitons in Honeycomb Photonic Lattices, Phys. Rev. Lett. **98**, 103901 (2007).

[47] J. Guglielmon and M. C. Rechtsman, Broadband Topological Slow Light Through Higher Momentum-Space Winding, Phys. Rev. Lett. **122**, 153904 (2019).

[48] S. Afzal, T. J. Zimmerling, Y. Ren, D. Perron, and V. Van, Realization of Anomalous Floquet Insulators in Strongly Coupled Nanophotonic Lattices, Phys. Rev. Lett. **124**, 253601 (2020).

[49] A. Shaltout, A. Kildishev, and V. Shalaev, Time-varying metasurfaces and Lorentz non-reciprocity, Opt. Mater. Express **5**, 2459 (2015).

[50] M. Mattheakis, C. A. Valagiannopoulos, and E. Kaxiras, Epsilon-near-zero behavior from plasmonic Dirac point: Theory and realization using two-dimensional materials, Phys. Rev. B **94**, 201404(R) (2016).

[51] T. F. Li, V. Nagai, D. H. Gracias, and J. B. Khurgin, Limits of imaging with multilayer hyperbolic metamaterials, Opt. Express **25**, 13588 (2017).

[52] Z. W. Guo, H. T. Jiang, and H. Chen, Hyperbolic metamaterials: From dispersion manipulation to applications, J. Appl. Phys. **127**, 071101 (2020).

[53] W. G. Song, H. M. Li, S. L. Gao, C. Chen, S. N. Zhu, and T. Li, Subwavelength self-imaging in cascaded waveguide arrays, Adv. Photon. **2**, 036001 (2020).

[54] T. Zhumabek and C. Valagiannopoulos, Light trapping by arbitrarily thin cavities, Phys. Rev. Res. **2**, 043349 (2020).